A Similarity Solutions Approach to Forced Convection via a Porous Medium Attached to Flat Plate

Augustine Akuoko Kwarteng*[1,2], Jose Corona[2], John Kizito[2]

[1]*Department of Mechanical Engineering, University of Mines and Technology, P.O. Box 237, Tarkwa, Ghana*

[2] *Department of Mechanical Engineering, North Carolina A&T State University, 1601 East Market St, Greensboro, NC 27411, U.S.A*

**Corresponding author*

***Abstract*: In the present study, a porous medium adjoining a heated flat plate was modelled by a similarity approach to determine the effect of porosity on the heat transfer phenomena. The momentum and energy equations for porous media transport were transformed using an appropriately determined similarity parameter. The solutions to the momentum equations proved to depend only on the porosity and not the material used. The energy equation however was additionally dependent on the combinations of fluid type and metal matrix used and was solved for four combinations; water/aluminum, air/aluminum, air/copper and SAE 20W-50/stainless. The results show that replacing the clear fluid control volume with a porous matrix altered both the velocity profiles and temperature distribution profiles at all Reynolds numbers. As the porosity of the medium decreased, it resulted in an increase in interfacial area as well as thermal diffusion in the direction normal to the plate, both of which was seen to enhance the heat transfer coefficients. Decreasing porosity also resulted in an increase in thermal storage as well a reduction in volume flow rate going through the medium, which on the other hand tend to inhibit convection. Thus, changing the porosity triggered effects on the heat transfer coefficient. This opposing trend favored convection at porosity greater than 0.5 for low Prandtl number fluids. The clear fluid condition has the lowest heat transfer coefficient and the values increased steeply as porosity changed from 0.99 through 0.7. The heat convection curve reached its maximum turning point at a porosity of 0.5 and then reversed in trend. The dimensionless heat transfer coefficient was found to fit the equation $h_L L/{Re_L}^{0.5} k_f Pr_f = a\varepsilon^b {Pr_m}^c$ ($a = 0.51966$; $b =$ 0.54683; $c = -0.665349$). Using Stanton number representation, the relation is $St{Re_L}^{1/2} = \frac{1}{3} a\varepsilon^b {Pr_m}^c$, which portrays in relative terms how the convection enhancement and the opposing thermal storage effects vary with porosity. This study concluded that implementing a porous structure in a medium is feasible for enhancing heat transfer performance.**

***Keywords*: porous media flow, local thermal equilibrium, convection enhancement, similarity solutions.**

Nomenclature

Velocity vector	$\mathbf{V}$
Velocity in x-direction	u
Velocity	v
Temperature	T
Pressure	P
Forccheimer constant or inertial coefficient	F
Absolute viscosity	μ
Kinematic viscosity	ν
Permeability	K
Porosity	ε
Darcy Number	Da
Reynolds number	Re
Pore scale Reynolds number	Re_p
Dimensionless heat transfer coefficient	h^*
Thermal conductivity	k
Thermal conductivity of fluid	k_f
Thermal Conductivity of Solid	k_s
Solid specific heat	C_s
Fluid specific heat	C_f
Thermal diffusivity	α
Dispersion coefficient Tensor	D_m
Dispersion coefficient for homogenous isotropic material	d_m
Fluid to solid thermal conductivity ratio	λ
Stream function	f
Dimensionless pressure	H
Dimensionless temperature	Θ
Wall Temperature	T_w
Bulk flow temperature	T_o
Thermal capacity ratio of fluid to porous medium	β
Representative elemental volume	REV
Volume	$\forall$

I. INTRODUCTION

Interest in porous media transport phenomena is driven by the growing applications of porous media transport models in areas such as thermal insulation, packed bed heat

exchangers, drying technology, catalytic reactors, petroleum industries, geothermal systems, and electronic cooling[1]. Porous bluff bodies can be designed to enhance gas mixing in reactors and combustors resulting in improved combustion efficiency and the combustion stability[2]. Flow in electronic devices using porous heat sinks, microcarriers or scaffolds in a bioreactor, liquid-solid reactors with settling of flocs of material, control rod arrangement in a nuclear reactor core and filters used in pharmaceutical and chemical industries rely on porous various media models[3].

Porosity is an important property of a porous media transport phenomena. It plays a direct role in altering the relative effects of the solid phase and fluid properties on the fluid dynamic and thermal transport properties. Geometrically, porosity represents the fraction of void volume to the entire volume of the porous medium. In packed beds, studies have shown that porosity has a dominant effect on the hydrodynamic properties and small changes in porosity results in significant changes in pressure drop requirements[4]. Knowing that the pressure field is intimately linked to the velocity field via the momentum equation, it can be inferred that the velocity field has the same level of sensitivity to changing porosity of the medium.

Review of contemporary literature in heat transfer reveals a good number of research works have focused on heat transfer enhancement[5, 6]. Metal foam heat exchangers have considerable advantages in thermal management and heat recovery over several commercially available heat exchangers[7]. Foams and foam-like materials have gained significant attention with the aim of predicting their heat transfer capabilities through direct measurement and thermo-structural modeling [8, 9]. In a good number of instances, volumetric heat transfer coefficients are determined for forced convection using the pore per inch or overall porosity, as the primary structural discriminator[5, 9]. The heat transfer capability of any particular foam was not however conclusively established based on porosity alone but models such as ordered rectilinear ligaments and unit cell-based approach, meet with some success in predicting the overall heat transfer rates [5, 10]. Tzer-Ming et al.[11] explored the effects of parameters such as the steady-state air preheating temperature ratio, Reynolds number and porosity of the medium on local and average heat transfer behavior of porous aluminum-foam heat sinks in a channel. They observed that the heat transfer enhancement ratio of using a porous heat sink in a channel to a hollow channel is far greater than unity and generally decreased with Reynolds number.

Karimi et al.[12] analytically studied forced convection in a channel partially filled with a porous material and subjected to constant wall heat flux subject to local thermal non-equilibrium boundary conditions. Their work acknowledged that a precise description of the interfacial thermal has been the subject of on-going research and is yet to fully evolve. The solutions obtained incorporated the dependence on porous material thickness, Darcy number, fluid to solid thermal conductivity ratio and Biot number as parameters. The results can be readily used to validate numerical simulations. Earlier work by Alzami and Vafai [1] investigated variants within porous media transport models. They identified four major categories namely constant porosity, variable porosity, thermal dispersion, and non-thermal equilibrium conditions. Their work evaluated the effect of the four variants and established conditions leading to convergence or divergence of different energy equation models. They concluded that variances in general, have a more pronounced effect on the velocity field and relatively smaller effects on the temperature field and Nusselt number distributions. Vafai and Thiyagaraja [13] obtained an accurate solution using a singular perturbation analysis. The closed-form analytical solution obtained showed a dependence of the velocity profiles and boundary layer thickness on inertia coefficient and pore scale Reynolds number. Nakayama and Pop[14] employed a local similarity transformation to a stationary plate problem for a forced through porous medium. They obtained asymptotic formulas for Nux as a function of the dimensionless streamwise coordinates and the dimensionless group comprising of the effective Prandtl number, porosity and streamwise coordinate.

This current study dives into the suitability of woven meshes of cylindrical wires as convection enhancement devices in a similar fashion to the usage of fins. The success of such a system will be measure by its ability to enhance, the heat transfer rate. This work set out to determine explicitly, the dependence of convection rates on porosity of seamless metallic foam adjoining a heated semi-infinite flat plate. A similarity approach is adopted for generalization, and also to save computational time. It was hypothesized that the introduction of solid structures extending from the surface of a heated flat plate into the flow could enhance the overall heat transfer rate by providing the surface with a direct path for conduction. Additionally, the network metallic wires extending into the medium presented additional interfacial area to the flow thereby promising a possibility of enhanced heat transfer from the heated substrate. It is the goal of this study to demonstrate explicitly, the effect of porosity on the convection phenomena and the hydrodynamic mechanisms resulting in such variation. The local thermal equilibrium energy equation was used along with the porous media momentum equation via a coordinate transformation approach to generate similarity solutions.

II. MATERIALS AND METHODS

A. Model and fundamental equations

As illustrated in figure 1, a flat plate with a matrix of metallic wires is subjected to wall heat flux. Flow is supplied from upstream at a steady velocity. The presence of the porous control volume and the adjoining heated plate alters the otherwise uniform velocity and temperature profile coming from upstream. The momentum and energy transport interaction are described in equations 1 and 2 respectively [15].

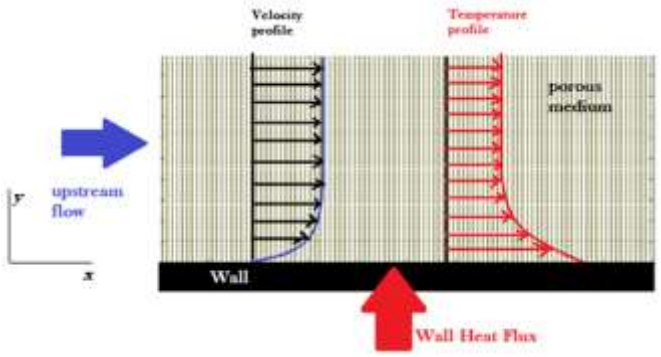

Figure 1: Schematic diagram describing flow through the porous medium

It is customary to model a porous medium from the macroscopic approach, but at the microscopic level we see a basic structure which can exhibit various symmetrical features, especially for materials that are engineered to be porous. Let us consider a medium consisting of packed bed of spherical balls or a network of cylindrical wires woven into the matrix as shown in Figure 2. Each configuration will have void characteristics based on the size of the balls or diameter of the cylindrical wires and length between adjacent joints. Taking an elemental volume, which is conveniently contains the basic cell or repeatable pattern of the entire medium, the porosity can be deduced from some knowledge how much of the solid matrix occupies that space. The concept here is analogous to atomic packing factor in material science. A unit cell approach affords one the ability to obtain the porosity of the medium as a function of the geometry, from which point the hydrodynamic analysis can proceed.

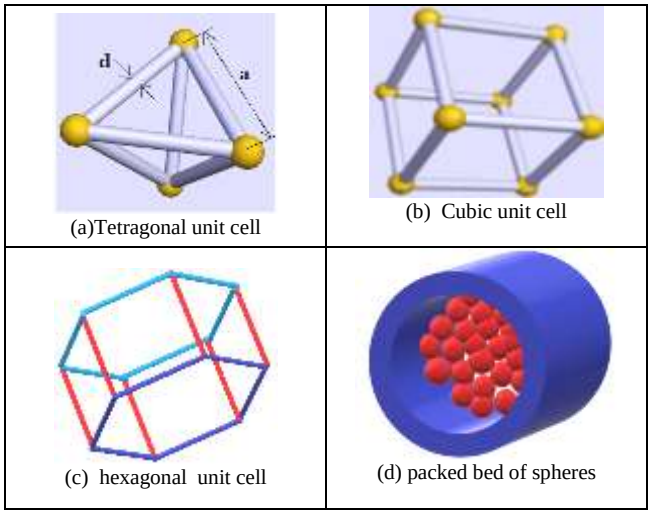

(a)Tetragonal unit cell

(b) Cubic unit cell

(c) hexagonal unit cell

(d) packed bed of spheres

Figure 2: basic lattice of selected porous media

$$\frac{\rho}{\varepsilon}\left(\frac{\partial \mathbf{V}}{\partial t}+\frac{1}{\varepsilon}\mathbf{V}\cdot\nabla\mathbf{V}\right)=-\nabla p-\frac{\mu}{K}\mathbf{V}-\frac{\rho F}{\sqrt{K}}\mathbf{V}|\mathbf{V}|+\frac{\mu}{\varepsilon}\nabla^2\mathbf{V} \quad (1)$$

$$\left(\rho_m C_m\frac{\partial T}{\partial t}+\rho_f C_f\mathbf{V}\cdot\nabla T\right)=\nabla.[k_m]\nabla T \quad (2)$$

$$where\ (\rho C)_m=\varepsilon(\rho C)_f+(1-\varepsilon)(\rho C)_s$$
$$and\ k_m=\varepsilon k_{0f}+(1-\varepsilon)k_s$$

B. Scaling Analysis

Scaling the momentum equation with the substitutions $u=U_o u^*;\quad v=U_o v^*;\quad p=\rho U_o{}^2 p*+p_o;\quad x=lx*;\quad y=ly*;$ yields equation 3. Equation 3 shows the relative significance of flow inertia, and hydraulic resistance via the Reynolds number Re, and the Darcy number Da.

$$\frac{1}{\varepsilon^2}\mathbf{V}\cdot\nabla\mathbf{V}=-\nabla p-\frac{1}{Da\,Re}\mathbf{V}-\frac{F}{\sqrt{Da}}\mathbf{V}|\mathbf{V}|+\frac{1}{Re_p\,\varepsilon}\nabla^2\mathbf{V} \quad (3)$$

$$\text{where } Da=\frac{K}{l^2} \text{ and } Re=\frac{\rho U_o l}{\mu}$$

Imposing a high porosity assumption on the porous structure, permeability of the medium is high relative to its pore scale length l, resulting in high Darcy numbers. In a non-Darcian flow, the Darcy term in the momentum equation is redundant as it only models the linear effect of flow velocity at low Reynolds number[15]. The so-called non-Darcy flow in porous media occurs if the flow velocity becomes large enough so that Darcy's law for the pressure gradient and the flow velocity is no longer valid [16]. The combination of the Forchheimer and Brinkmann terms adequately describe the momentum distribution at over a wide range of Reynolds numbers.

Far out in the stream away from the flat plate, the velocity gradients diminish as the flow gets to a steady bulk velocity resulting in equation 4.

$$-\nabla p-\frac{F}{\sqrt{Da}}\mathbf{V}|\mathbf{V}|=0 \quad (4)$$

The momentum boundary layer typically covers a very thin region compared to the entire control volume. Thus, equation 4 is applicable everywhere in the domain. Additionally, the boundary layer region must satisfy equation 5 because of the significant effects of velocity gradients near the wall.

$$\frac{1}{\varepsilon^2}\mathbf{V}\cdot\nabla\mathbf{V}=\frac{1}{Re\,\varepsilon}\nabla^2\mathbf{V} \quad (5)$$

As the current study is focused on developing a similarity-based approach for the problem at hand, we will revert to the starting versions of equations 4 and 5, labelled as 4b and 5b respectively.

$$-\nabla p-\frac{\rho F}{\sqrt{K}}\mathbf{V}|\mathbf{V}|=\mathbf{0} \quad (4b)$$

$$\frac{\rho}{\varepsilon^2}\mathbf{V}\cdot\nabla\mathbf{V}=\frac{\mu}{\varepsilon}\nabla^2\mathbf{V} \quad (5b)$$

C. Similarity solutions and coordinate transformation

From 5b the x-momentum equation was nondimensionalized as follows.

$$\frac{\rho}{\varepsilon^2}\left(u\frac{\partial u}{\partial x}+v\frac{\partial u}{\partial y}\right)=\frac{\mu}{\varepsilon}\frac{\partial^2 u}{\partial y^2} \quad (6a)$$

$$\frac{\rho U_o^{\,2}}{X\varepsilon^2}u\frac{\partial u}{\partial x}+\frac{\rho U_o^{\,2}}{Y\varepsilon^2}v\frac{\partial u}{\partial y}=\frac{U_o\mu}{\varepsilon Y^2}\frac{\partial^2 u}{\partial y^2} \qquad (6b)$$

$$\frac{\rho U_o^{\,2}}{x\varepsilon^2}\sim U_o\frac{\mu}{\varepsilon y^2} \qquad (6c)$$

$$y\sim\left(\frac{\varepsilon\nu x}{U_o}\right)^{1/2} \qquad (6d)$$

$$\eta=y\varepsilon^{1/2}\sqrt{\frac{U_o}{\nu x}} \qquad (6e)$$

A factor of 2 is introduced in the denominator to shorten the range of η required for the solutions to reach infinity conditions. Hence the parameter used is the transformation is the form in equation 6f. $\varepsilon^{1/2}$ is conveniently written as D_K to allow for subsequent formulations of the similarity equations with alternate combinations of the porous media properties. For instance, combining equation 6d with the dimensionless numbers in equation 3, results in $\eta = yDa^{-1/2}\sqrt{U_o/2\nu x}$ as the most appropriate transformation variable for low porosity flows (when Da is significantly low).

$$\eta=y\varepsilon^{1/2}\sqrt{\frac{U_o}{2\nu x}} \qquad (6f)$$

Using the equations 6g and 6h, the x-momentum equation proceeds as follows as detailed in equations 7a through 7c.

$$u=U_o f';\ v=\frac{1}{2}D_k\left(\frac{2U_o\nu}{x}\right)^{\frac{1}{2}}(\eta f'-f);\quad \frac{T-T_o}{T_w-T_o}=\Theta \qquad (6g)$$

$$\eta=yD_K\sqrt{\frac{U_o}{2\nu x}};$$

$$\frac{\partial\eta}{\partial x}=-\frac{\eta}{2x};\quad \frac{\partial\eta}{\partial y}=\frac{\eta}{y};$$

$$\frac{\partial x}{\partial y}=-\frac{2x}{y};\qquad \frac{\partial y}{\partial x}=-\frac{y}{2x} \qquad (6h)$$

$$\frac{\rho}{\varepsilon^2}\left(u\frac{\partial u}{\partial x}+v\frac{\partial u}{\partial y}\right)=\frac{\mu}{\varepsilon}\frac{\partial^2 u}{\partial y^2} \qquad (7a)$$

$$\frac{\rho}{\varepsilon^2}\left(-U_o f''U_o f''\frac{\eta}{2x}+\frac{1}{2}D_k\left(\frac{2U_o\nu}{x}\right)^{\frac{1}{2}}(\eta f'-f)U_o f''\frac{\eta}{y}\right)=\frac{\mu}{\varepsilon}U_o f'''\left(\frac{\eta}{y}\right)^2 \qquad (7b)$$

$$-\frac{1}{\varepsilon D_k^{\,2}}nf'f''+\frac{1}{\varepsilon}nf'f''-\frac{1}{\varepsilon}ff''=f''' \qquad (7c)$$

The energy equation proceeds as follows.

$$\left(\frac{\partial T}{dt}+\frac{\rho_f C_f}{\rho_m C_m}u\frac{\partial T}{\partial x}+\frac{\rho_f C_f}{\rho_m C_m}v\frac{\partial T}{\partial y}\right)=\frac{\overline{k_m}}{\rho_m C_m}\left(\frac{\partial^2 T}{\partial x^2}+\frac{\partial^2 T}{\partial y^2}\right) \qquad (8a)$$

$$\left(\frac{\partial T}{dt}+\beta u\frac{\partial T}{\partial x}+\beta v\frac{\partial T}{\partial y}\right)=\overline{\alpha_m}\left(\frac{\partial^2 T}{\partial x^2}+\frac{\partial^2 T}{\partial y^2}\right) \qquad (8b)$$

Under steady conditions the transient term drops from equation 8b. Transforming equation 8c using the definitions in 6g and 6h yields equation 8d for the energy equation.

$$\beta u\frac{\partial T}{\partial x}+\beta v\frac{\partial T}{\partial y}=\overline{\alpha_m}\frac{\partial^2 T}{\partial y^2} \qquad (8c)$$

$$\eta f'\Theta'\left(1-\frac{1}{D_K^{\,2}}\right)-f\Theta'=D_k^{\,2}\frac{\overline{\alpha_m}}{\beta\nu_f}\Theta''$$

It can be shown that $\frac{\overline{\alpha_m}}{\beta\nu}=\left(\frac{k_d}{k_f}+\frac{1-\varepsilon}{\lambda}+\varepsilon\right)\frac{1}{Pr_f}$

$$\eta f'\Theta'\left(1-\frac{1}{D_K^{\,2}}\right)-f\Theta'=\left(\frac{k_d}{k_f}+\frac{1-\varepsilon}{\lambda}+\varepsilon\right)\frac{1}{Pr_f}\Theta'' \qquad (8d)$$

If u in equation 6 is chosen such that $u=D_k^{\,2}U_o f'$, the equations of motion reduce to 9 and 10 for the momentum and energy equations respectively. Equations set 7c and 8d proved to have the solutions with the set 9 and 10 when transposed back to the domain of native variables. For convenience, the study proceeds with the set in 9 and 10. It can be observed at a glance that if porosity is assigned a value equal to 1, the similarity equations 9 and 10 become the Blasius equations [17]. The solution for the momentum equation is seen to depend only on the porosity of the solid matrix. The energy equation on the other hand, depends on the Prandtl number of the fluid, thermal conductivity ratio of the fluid to solid, dispersion, porosity as well as a coupling from the momentum equation as f.

$$-ff''=\varepsilon f''';\qquad f(0)=0;f'(\infty)=0 \qquad (9)$$

$$-f\Theta'=\left(\frac{k_d}{k_f}+\frac{1-\varepsilon}{\lambda}+\varepsilon\right)\frac{1}{Pr_f}\Theta'';\quad \Theta(0)=1;\Theta(\infty)=0 \qquad (10)$$

For convenience, the ratio $Pr_f/\left(\frac{k_d}{k_f}+\frac{1-\varepsilon}{\lambda}+\varepsilon\right)$ is designated as a modified Prandtl number, Pr_m which quantitatively describes the extent to which the introduction of a matrix of metallic structures affects the thermal characteristics of the otherwise clear fluid domain [20]. Equation 10 is rewritten compactly as 10b.

$$-fPr_m\Theta'=\Theta'';\qquad \Theta(0)=1;\Theta(\infty)=0 \qquad (10\,b)$$

The results presented and discussed in the next section features solutions for the momentum equation for porosity values from 0.1 through 0.99. The energy equation was solved for two flow systems: first comprising water and aluminum matrix, and later for air and aluminum matrix. The choice of fluids for demonstration was made bearing in mind that air has Prandtl number less than 1 whilst water has Prandtl number greater than 1. Additionally, the thermal conductivity ratios are orders of magnitude apart. A water – aluminum convection system has $\lambda = 2.36\times10^{-3}$ at 30^oC whilst air - aluminum has $\lambda = 1.11\times10^{-4}$. Solutions for the clear fluid condition was as well included as a baseline for comparison. Additional runs were made with SAE 20W-50 oil flowing through a stainless, and finally air flowing through a porous mesh of copper. In all, four combinations of fluid-metallic

systems were studied, with choices carefully made to demonstrate common cooling applications.

D. Temperature gradients, heat transfer rate and Nusselt number relationships

Wall heat flux is obtained from the conduction rate at y=0 as shown in the proceeding steps from equation 11. The heat transfer rates in terms of local Nusselt number and local heat transfer coefficient is given in equation 12.

$$q_w = -k_m \frac{dT}{dy}\Big|_{y=0}$$

$$q_w = -k_m \frac{\partial T}{\partial y}\frac{\partial \eta}{\partial y}\Big|_{y=0}$$

$$q_w = -k_m (T_w - T_e)\Theta'(0)\frac{\eta}{y} \tag{11}$$

$$q_w = h_x (T_w - T_o)$$

$$h_x (T_w - T_o) = -k_m (T_w - T_o)\Theta'(0)\mathrm{D_k}\left(\frac{\mathrm{U_o}}{2xv}\right)^{\frac{1}{2}}$$

Introducing the local Nusselt number as,

$$\frac{Nu_x k_m}{x} = h_x = -k_m \Theta'(0)\mathrm{D_k}\left(\frac{\mathrm{U_o}}{2xv}\right)^{\frac{1}{2}} \tag{12}$$

$$\frac{Nu_x k_m}{{Re_x}^{1/2}} = \frac{h_x x}{{Re_x}^{1/2}} = -\frac{k_m \Theta'(0)\mathrm{D_k}}{\sqrt{2}} {Re_x}^{\frac{1}{2}}$$

$$\frac{Nu_x}{{Re_x}^{1/2} Pr_m} = \frac{h_x x}{{Re_x}^{1/2} Pr_f k_f} = -\frac{\Theta'(0)\mathrm{D_k}}{Pr_m \sqrt{2}} \tag{13}$$

where

$$Pr_m = \frac{Pr_f}{\left(\frac{\mathrm{k_d}}{\mathrm{k_f}} + \frac{1-\varepsilon}{\lambda} + \varepsilon\right)} \; and \; k_m = \left(\frac{\mathrm{k_d}}{\mathrm{k_f}} + \frac{1-\varepsilon}{\lambda} + \varepsilon\right) k_f \tag{14}$$

$$\frac{Nu_x}{{Re_x}^{1/2} Pr_m} = \frac{h_x x}{{Re_x}^{1/2} Pr_f k_f} = -\frac{\Theta'(0)\mathrm{D_k}}{Pr_m \sqrt{2}} \tag{15}$$

Average values of Nusselt number and heat transfer coefficient over the entire plate are obtained from integrating equation 15 over the entire length L.

$$\frac{\overline{Nu_L}}{Pr_m} = -\frac{1}{L}\int_0^L \frac{\Theta'(0)\mathrm{D_k}}{Pr_m \sqrt{2}}\left(\frac{\mathrm{U_o} x}{v}\right)^{\frac{1}{2}} dx$$

$$\frac{\overline{Nu_L}}{{Re_L}^{1/2} Pr_m} = -\frac{\mathrm{D_k}\sqrt{2}}{3Pr_m}\Theta'(0) \tag{16}$$

$$\frac{\overline{Nu_L}}{{Re_L}^{1/2} Pr_m} = -\frac{\varepsilon^{\frac{1}{2}}\sqrt{2}}{3Pr_m}\Theta'(0) \tag{17}$$

From the definition of Stanton number, $St = \frac{Nu}{PrRe}$, the ratio $\frac{Nu}{PrRe_L{}^{1/2}}$ is recognized as $StRe_L{}^{1/2}$.

Thus, it can be concluded that

$$StRe_L{}^{1/2} = -\frac{\varepsilon^{\frac{1}{2}}\sqrt{2}}{3Pr_m}\Theta'(0) \tag{18}$$

Similarly, the average heat transfer coefficient proceeds from equation 15 as follows.

$$\frac{h_x x}{{Re_x}^{1/2} Pr_f k_f} = -\frac{\mathrm{D_k}}{Pr_m \sqrt{2}}\Theta'(0)$$

$$\frac{\overline{h_L}}{Pr_f k_f} = -\frac{1}{L}\int_0^L \frac{\Theta'(0)\mathrm{D_k}}{Pr_m \sqrt{2}}\frac{1}{x}\left(\frac{\mathrm{U_o} x}{v}\right)^{\frac{1}{2}} dx$$

$$\frac{\overline{h_L} L}{Pr_f k_f {Re_L}^{1/2}} = -\frac{\Theta'(0)\mathrm{D_k}\sqrt{2}}{Pr_m} \tag{19}$$

$$\frac{\overline{h_L} L}{Pr_f k_f {Re_L}^{1/2}} = -\frac{\varepsilon^{\frac{1}{2}}\sqrt{2}}{Pr_m}\Theta'(0) \tag{20}$$

From equations 17and 20, the average heat transfer coefficient can be related to the average Nusselt number as in equation 21.

$$\frac{\overline{h_L} L}{Pr_f k_f {Re_L}^{1/2}} = \frac{3\overline{Nu_L}}{{Re_L}^{1/2} Pr_m}$$

$$\overline{h_L} = \frac{3\overline{Nu_L} k_f}{L}\left(\frac{\mathrm{k_d}}{\mathrm{k_f}} + \frac{1-\varepsilon}{\lambda} + \varepsilon\right) \tag{21}$$

E. Grid Independence and convergence

The boundary value problem in equations set 9 and 10 were discretized and solve for water flowing through an aluminum matrix at a porosity of 0.9. The solutions at varying $\delta\eta$ is presented in Figure 3. The solution show convergence for $\delta\eta \leq 0.001$ and thus the solutions in this study proceed with a grid spacing of 0.001.

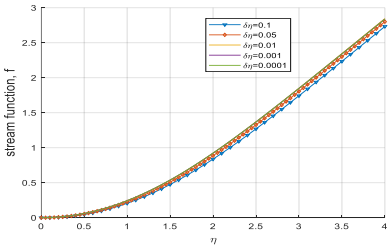

a) Stream functions

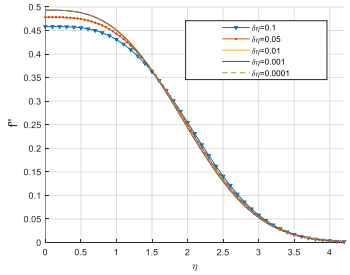

b) f''

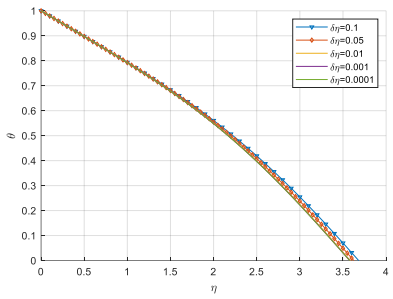

c) temperature profile

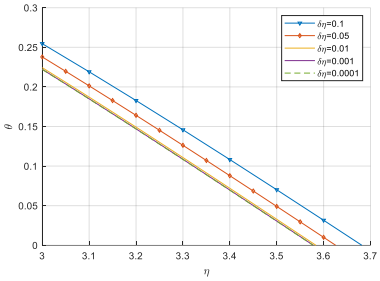

d) temperature profile zoomed in

Figure 3: Grid independence studies at porosity of 0.9

III. RESULTS AND DISCUSSION

The equations modelled in this study were programmed and solved using MATLAB®. Figures 4 through 6 show the results of the momentum solution. The graphs depict clear dependence of the stream functions, dimensionless velocities, and velocity gradients on porosity. The momentum solution becomes a vital input for the energy equation since it has a coupling to the dimensionless energy equation via f.

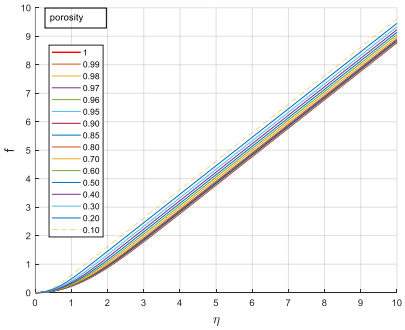

Figure 4: solution of stream functions (f)

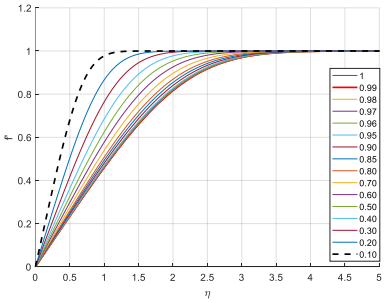

Figure 5: dimensionless velocity (f')

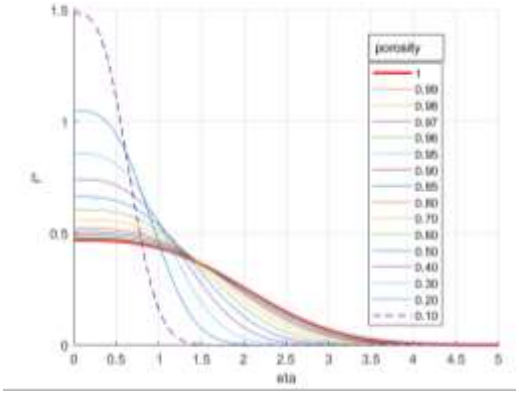

Figure 6: dimensionless velocity gradients (f'')

Figure 7 shows the temperature profiles for at various porosities for a system that runs water through a matrix of aluminum mesh. The process also repeated for air and aluminum is presented in Figures 10 through 12.

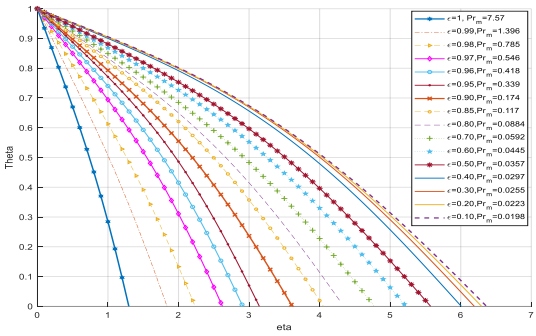

Figure 7: Temperature Profile with water-based coolant through a porous aluminum matrix ($\lambda = 0.00236, Pr = 7.57, kf = 0.56$)

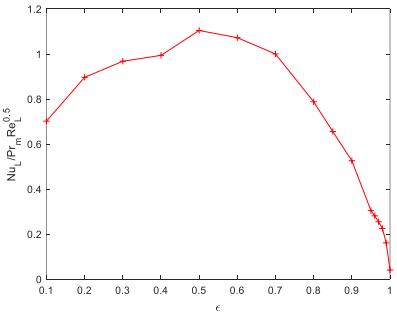

Figure 8: $Nu/Pr_m Re_L^{1/2}$ vs porosity for porous aluminum material and water-based coolant convection system

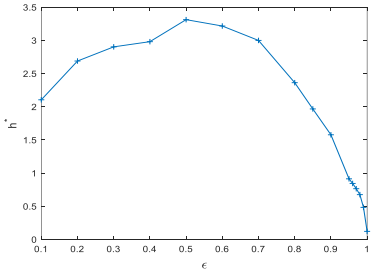

Figure 9: dimensionless heat transfer coefficient $\bar{h}L/k_f Pr_f Re_L^{0.5}$ vs porosity for porous aluminum material and water-based coolant convection

The form of the dimensionless energy equation stipulates a dependence of the energy equation solution on porosity and modified Prandtl number of the medium which is also a function of thermal conductivity ratio λ, porosity, the fluid's Prandtl number and dispersion. To ascertain the above-mentioned dependence, the solution process was repeated with air flowing through the aluminum matrix attached to the heated flat plate. The solutions for air/aluminum as displayed in Figures 9 through 11 showed a similar trend of results as was obtain for the water-cooling medium. When the convection system was changed to SAE 20W-50 and stainless steel ($\lambda = 0.0094, \mathrm{Pr} = 1993, \mathrm{kf} = 0.141\ \mathrm{W/mK}$), a similar trend of Nusselt number relationship was observed as found in the aluminum -air, aluminum- water system. At a glance, the obvious striking difference is that the steel/SAE 20W system has a peak Nusselt number at a porosity of 0.3 whilst the aluminum-based medium has its peak at a porosity of 0.5 (compare Figures 11 and 13).

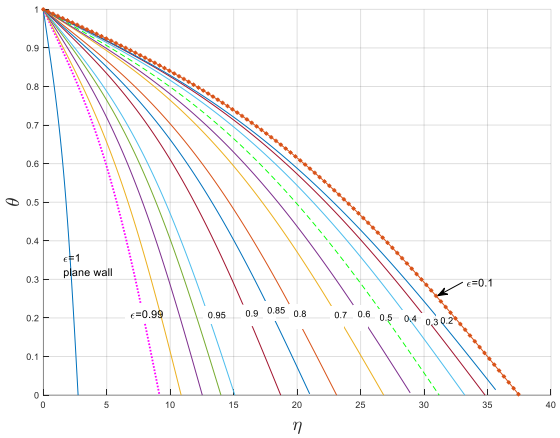

Figure 10: Temperature profile θ vs eta for various porosities for air flowing through aluminum matrix $(\lambda = 0.000111, \mathrm{Pr} = 0.7, \mathrm{kf} = 0.0262)$

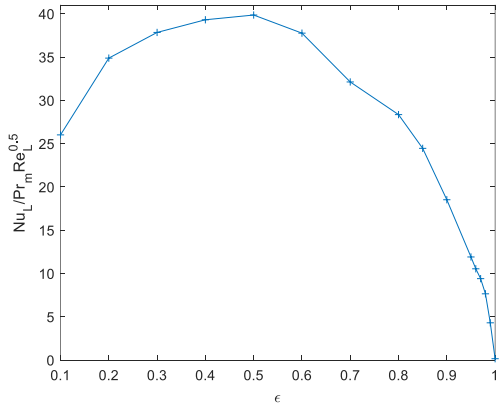

Figure 11: $\mathrm{Nu}/\mathrm{Pr}_m\mathrm{Re}_L^{1/2}$ vs porosity for air flowing through aluminum matrix $(\lambda = 0.000111, \mathrm{Pr} = 0.7, \mathrm{kf} = 0.0262)$

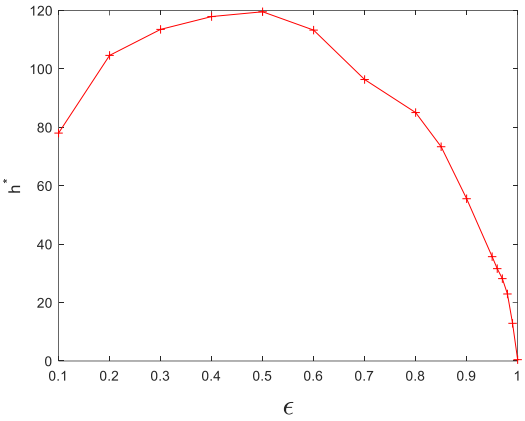

Figure 12: Dimensionless Heat transfer coefficient $\bar{h}L/k_l\mathrm{Pr}_l\mathrm{Re}_L^{0.5}$ vs porosity for air flowing through porous aluminum matrix $(\lambda = 0.000111, \mathrm{Pr} = 0.7, \mathrm{kf} = 0.0262)$

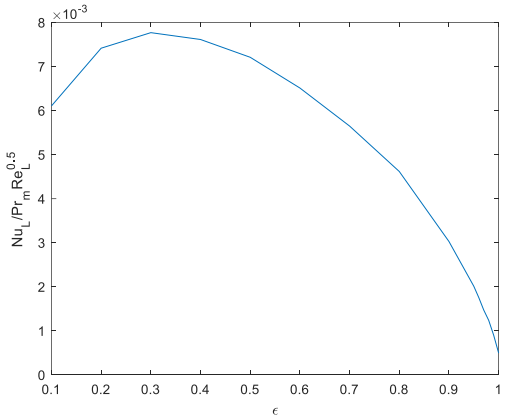

Figure 13: $\mathrm{Nu}/\mathrm{Pr}_m\mathrm{Re}_L^{1/2}$ vs porosity for SAE 20W-50 oil/stainless steel

The Nusselt number ratios for the various convection systems have varying order of magnitudes as observed in Figures 8, 11 and 13. It was instructive to do the overall comparison on a log scale plot as 14. When either copper or aluminum is cooled using air, the Nusselt numbers have the comparable order of magnitudes, thus both were presented on one graph in linear scale as in Figure 15.

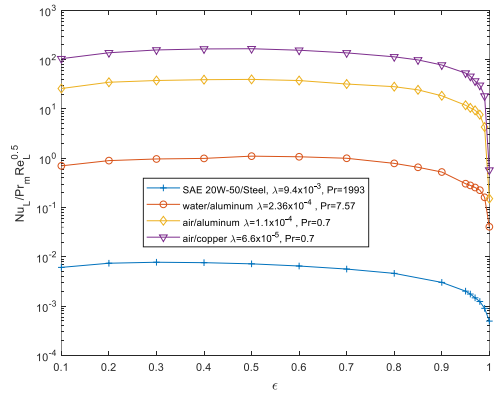

Figure 14: Comparing $\mathrm{Nu}_L/\mathrm{Pr}_m\mathrm{Re}_L^{0.5}$ vs porosity plots for the four convection systems under study

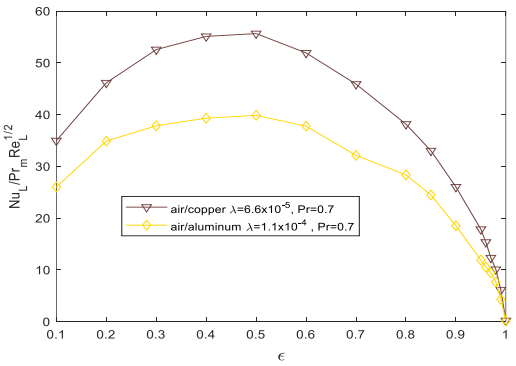

Figure 15 : $Nu_L/Pr_mReL^{0.5}$ vs porosity for air/copper and air/aluminum convection system

As observed from the data in table 1 $h^* = h^*(\Theta_o')$ and $\Theta_o' = \Theta_o'(\varepsilon, P_{rm})$.

Thus $h^* = h^*(\varepsilon, P_{rm})$. The dimensionless heat transfer coefficient for the water-cooled and air-cooled porous systems were found to fit the equation ${h_L L/Re_L}^{0.5} k_f Pr_f = a\varepsilon^b {Pr_m}^c$ $(a = 0.5197;\ b = 0.5468; c = -0.6653)$. Using Stanton number representation, the relation is ${StRe_L}^{1/2} = \frac{1}{3} a\varepsilon^b {Pr_m}^c$, which portrays in relative terms how the convection enhancement and the opposing thermal storage effects vary with porosity.

Table 1: Shows porosity, corresponding Prandtl numbers and wall temperature gradients

porosity	$= \frac{Pr_m}{Pr_f}$ $\left(\frac{k_d}{k_f} + \frac{1-\varepsilon}{\lambda} + \varepsilon\right)$	$\Theta'(0)$	$= -\frac{h^*}{\varepsilon^{1/2}\sqrt{2}} Pr_m \Theta'(0)$
1	7.5700	-0.65426	0.1222
0.99	1.3961	-0.48023	0.4840
0.98	0.7849	-0.37902	0.6760
0.97	0.5459	-0.30002	0.7654
0.96	0.4185	-0.25503	0.8444
0.95	0.3393	-0.22503	0.9142
0.9	0.1743	-0.20505	1.5780
0.85	0.1173	-0.17705	1.9678
0.8	0.0884	-0.16516	2.3635
0.7	0.0592	-0.15012	3.0003
0.6	0.0445	-0.13072	3.2174
0.5	0.0357	-0.11814	3.3134
0.4	0.0297	-0.09915	2.9816
0.3	0.0255	-0.09561	2.9033
0.2	0.0223	-0.09498	2.6898
0.1	0.0199	-0.0935	2.1055

From the relationship in equation 21 and the fitted equation (${h_L L/Re_L}^{0.5} k_f Pr_f = a\varepsilon^b {Pr_m}^c$), the solution is obtained in terms of Nusselt as in equation 22. Figures 16 through 18 shows how well the computational data fits into the approximating model.

$$Nu_L = 0.1732 {Re_L}^{0.5} Pr^{0.3347} \frac{\varepsilon^{0.5468}}{\left(\frac{1-\varepsilon}{\lambda} + \varepsilon\right)^{0.3347}} \quad (22)$$

The SAE 20W-50 based system, however, had different approximating constants from the others $(a = 0.4023;\ b = 0.3347; c = -0.7339)$. The corresponding Nusselt number relationship was obtained as given equation 23. The main distinguishing feature for the SAE 20W-50 system is the high Prandtl number of 1993.

$$Nu_L = 0.1341 {Re_L}^{0.5} Pr^{0.2661} \frac{\varepsilon^{0.3347}}{\left(\frac{1-\varepsilon}{\lambda} + \varepsilon\right)^{0.2661}} \quad (23)$$

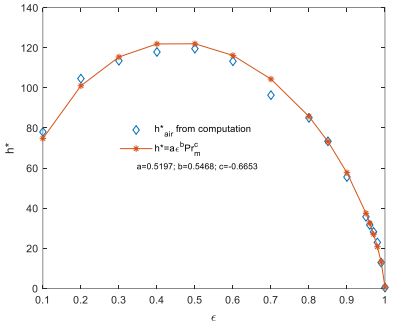

Figure 16: Comparing similarity results for air/aluminum convection to the approximating equation

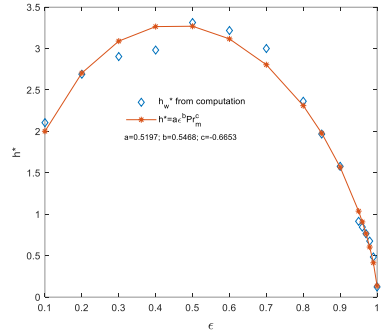

Figure 17: Comparing similarity results for water/aluminum convection to the approximating equation

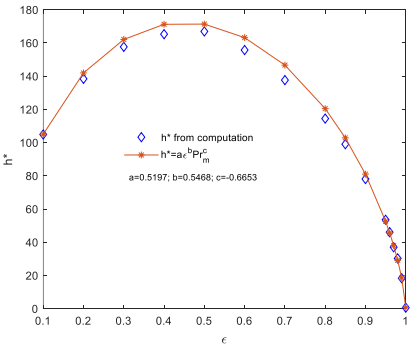

Figure 18: Comparing similarity results for copper/air convection to the approximating equation

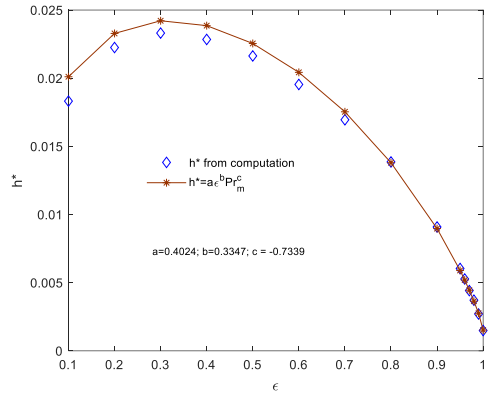

Figure 19: Comparing similarity results for SAE 20W-50 /stainless steel convection to the approximating equation

Data for the average heat transfer coefficients was transposed from the similarity solution and illustrated in Figure 20 and 21 for selected Reynolds numbers. From Figures 20 and 21, it is evident that liquid cooling can provide higher convection rates than gases at the same Reynolds numbers and porosity. Thermophysical properties of the fluids and metals used in this section are read from Engineering Toolbox[18] with the exception of SAE 20W-50 which was read from Thermal-Fluids Central [19]. The tables and illustrations that follow from this point is intended to portray a real feel of the results in terms of native parameters such as average heat transfer coefficients, velocity and temperature profiles within the domain for specified cases.

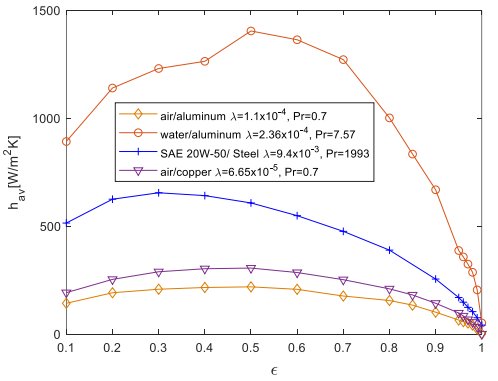

Figure 20: heat transfer coefficients at $Re_L=10^4$

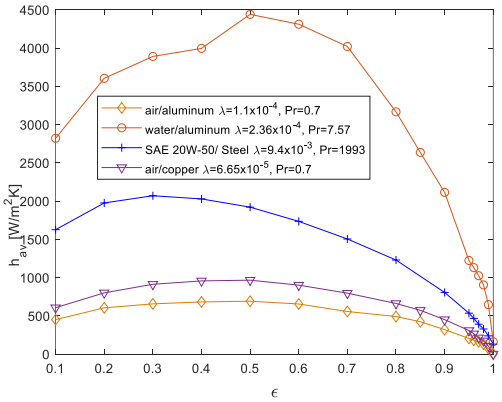

Figure 21: heat transfer coefficients at $Re_L=10^5$

Velocity and temperature contour plots at Reynolds Number $Re_L=2.5x10^5$ are respectively displayed for air going through aluminum matrix $(\lambda = 1.11x10^{-4}, Pr = 0.7, kf = 0.0262)$ in Figures 22 and 23. Observing the velocity contours, the thickness of the boundary layer was approximately the same for all values of porosity at constant Reynolds number. However, for lower porosities, a zone of near zero velocities develops at the entrance near the wall surface. This blue zone at the entrance grows taller as porosity decreases, and it has a physical representation of a blockage that forms at the entry. The temperature contours showed an increasing thermal boundary layer thickness with decreasing porosity.

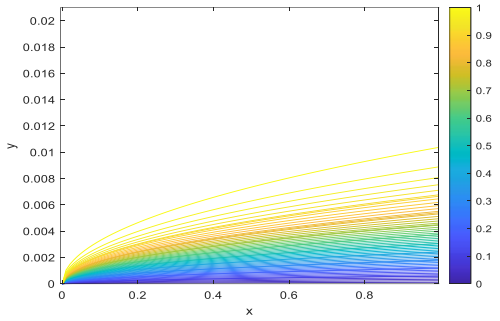

Figure 22a: u/U_∞ velocity contour plots in x-y domain for porous medium ,Clear fluid (porosity=1)

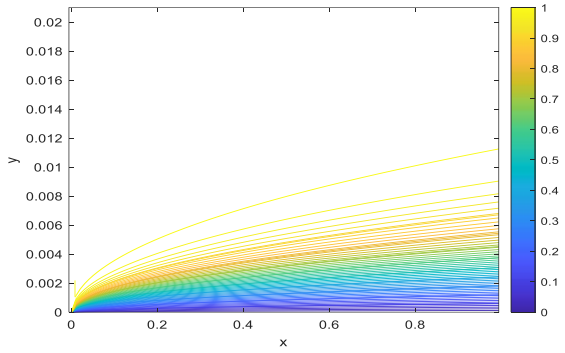

Figure 23b: u/U_∞ velocity contour plots in x-y domain for porous medium (porosity=0.99)

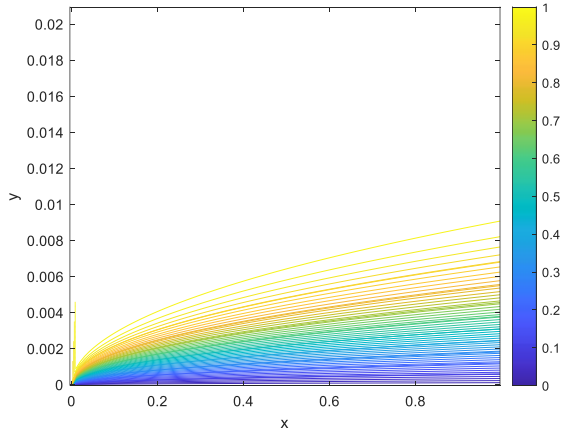

Figure 24c: u/U_∞ velocity contour plots in x-y domain for porous medium (porosity=0.9)

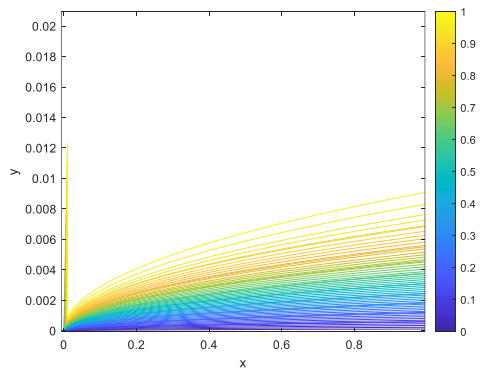

Figure 25d: u/U_o velocity contour plots in x-y domain for porous medium (porosity=0.9)

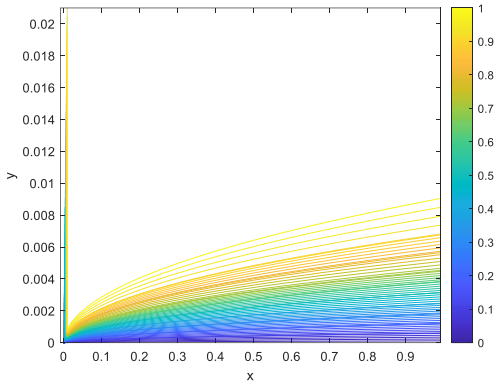

Figure 26b: u/U_o velocity contour plots in x-y domain for porous medium (porosity=0.2)

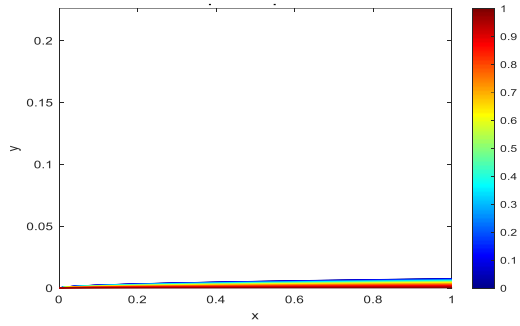

Figure 27a: Dimensionless Temperature Contours at $Re_L = 10^5$ air/ aluminum porous medium (clear fluid)

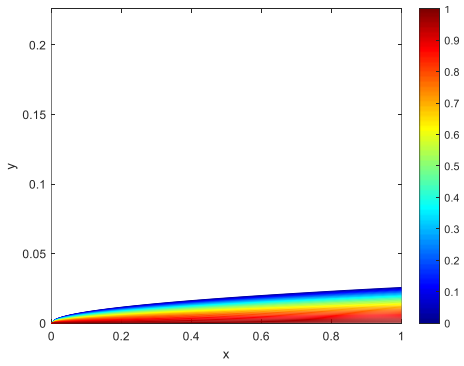

Figure 28b: Dimensionless Temperature Contours at $Re_L = 10^5$ air/ aluminum porous medium (porosity=0.99)

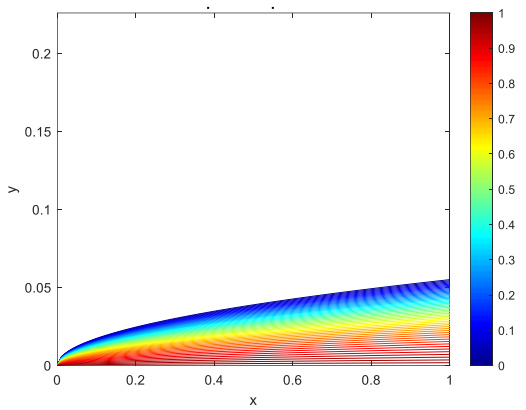

Figure 29c: Dimensionless Temperature Contours at $Re_L = 10^5$ air/ aluminum porous medium (porosity=0.90)

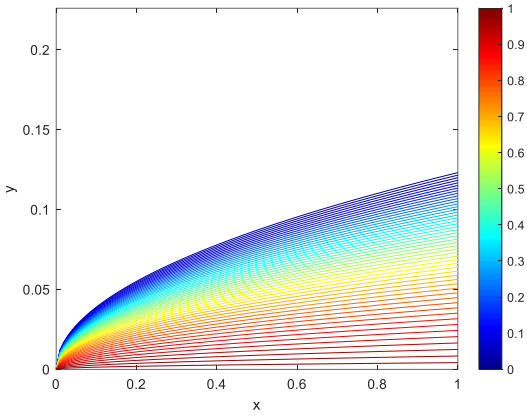

Figure 30d: Dimensionless Temperature Contours at $Re_L = 10^5$ air/ aluminum porous medium (porosity=0.5)

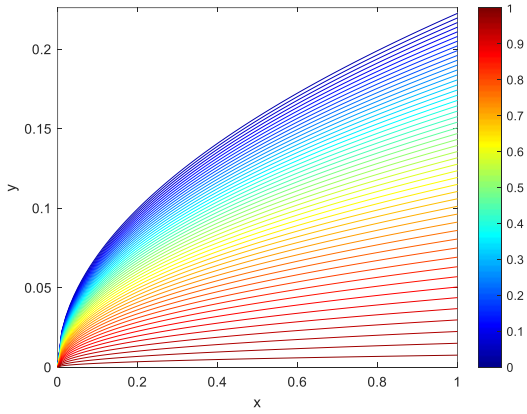

Figure 31e: Dimensionless Temperature Contours at $Re_L = 10^5$ air/ aluminum porous medium (porosity=0.2)

D. Validating velocity profile and Nusselt Number relation

A porous medium comprising of thin cylinders in a cubical pattern, with wire length $a = 5mm$ and diameter $d = 1mm$, the corresponding porosity is 0.9 was used to generate data for validation. Applying the Karman Cozeny equation yields a permeability of $K = 2.26 \times 10^{-6}\ m^2$. A graph of dimensionless velocity profile u/U_o on the abscissa vs dimensionless height $Y = y/\sqrt{K/\varepsilon}$ is shown in Figure 24

and compared with results from the by the exact solution by Vafai and Thiyagaraja [13]. In Figure 25, Nusselt number relationship in obtained from this present study (equation 22) is compared with results of the similarity solution from Nayakama and Pop ($Nu_x = \sqrt{\varepsilon Pr_e/\pi}$) .

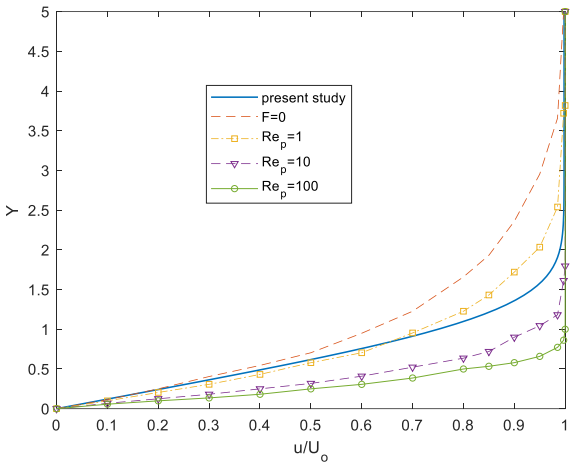

Figure 32: Validating dimensionless velocity profiles

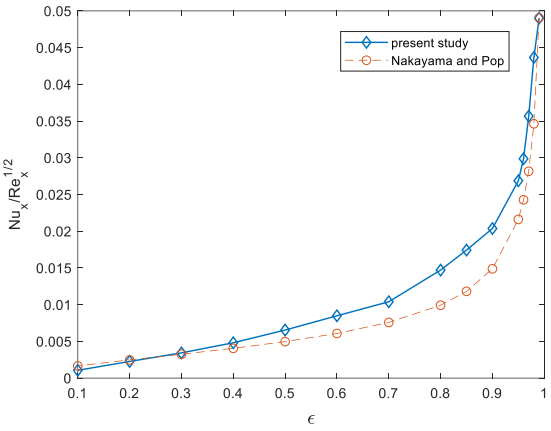

Figure 33: comparing the Nusselt number plot with similarity solutions from Nakayama and Pop[14]

IV. CONCUSION

The study has demonstrated explicitly the dependence of convection performance of a heated flat plate on the porosity of an adjoining metal matrix. Well-defined correlations have been shown to exist between the overall heat transfer indicators and porosity for four combinations of fluid and metal matrix. The clear fluid condition has the lowest heat transfer coefficient and the values increased steeply as porosity changed from 0.99 through 0.7. For low Prandtl number fluids, the heat convection curve reached its maximum turning point at a porosity of 0.5 and then reversed in trend. This dependence was represented explicitly by two major effects namely; the porosity and the modified Prandtl number of the porous medium as $StRe_L^{1/2} = \frac{1}{3}a\varepsilon^b Pr_m^c$ ($a = 0.51966;\ b = 0.54683;\ c = -0.665349$). Using Stanton number relation portrays in relative terms how the convection enhancement and the opposing thermal storage effects vary with porosity and Prandtl number of the medium.

It was concluded that implementing a porous structure in a medium is feasible for enhancing heat transfer coefficients. For instance, at a porosity of 0.85 and 0.7, the dimensionless heat transfer coefficient is respectively 16 times and 25 times higher compared to a flat plate without any adjoining porous structure. Porosity of the adjoining metal matrix has been demonstrated to alter the flow behavior in terms of the stream functions and derivatives, resulting in a compounding influence on the convective heat transfer phenomena. For water and air-cooled systems (having Prandtl numbers 7.57 and 0.7 respectively), the variation of thermal performance with porosity in terms of average Nusselt numbers was found to satisfy $\overline{Nu_L} = 0.1732\,Re_L^{0.5} Pr^{0.3347} \frac{\varepsilon^{0.5468}}{\left(\frac{1-\varepsilon}{\lambda}+\varepsilon\right)^{0.3347}}$. When using low Prandtl number fluids like water and air as coolant, the peak Nusselt number occurred when porosity is 0.5. Using SAE 20W-50 (with Pr =1993) resulted in a similar trend but different values of indices for Prandtl number and porosity-based terms in the variation; $\overline{Nu_L} = 0.1341\,Re_L^{0.5} Pr^{0.2661} \frac{\varepsilon^{0.3347}}{\left(\frac{1-\varepsilon}{\lambda}+\varepsilon\right)^{0.2661}}$. The peak Nusselt number shifted to a position corresponding to a porosity of 0.3.

REFERENCES

[1] Alazmi, B. and K. Vafai, Analysis of Variants Within the Porous Media Transport Models. Journal of Heat Transfer, 1999. **122**(2): p. 303-326.

[2] Yen, S.C.P., Y.L.; San, K.C., Design of a Porous Bluff-Body Disc on Improving the Gas-Mixing Efficiency. Proceedings of the World Congress on Engineering, 2017. **II**(WCE 2017): p. 1003-1007.

[3] Anirudh, K. and S. Dhinakaran, Effects of Prandtl number on the forced convection heat transfer from a porous square cylinder. International Journal of Heat and Mass Transfer, 2018. **126**: p. 1358-1375.

[4] Abbas, M.N., Modeling Of Porosity Equation For Water Flow Through Packed Bed Of Monosize Spherical Packing. Journal Of Engineering And Development, 2011. **15**(4): p. 205-226.

[5] Goldstein, R.J., et al., Heat transfer—A review of 2005 literature. International Journal of Heat and Mass Transfer, 2010. **53**(21): p. 4397-4447.

[6] Goldstein, R.J., et al., Heat transfer—A review of 2004 literature. International Journal of Heat and Mass Transfer, 2010. **53**(21): p. 4343-4396.

[7] Mahjoob, S. and K. Vafai, A synthesis of fluid and thermal transport models for metal foam heat exchangers. International Journal of Heat and Mass Transfer, 2008. **51**(15): p. 3701-3711.

[8] Dukhan, N., et al., One-dimensional heat transfer analysis in open-cell 10-ppi metal foam. International Journal of Heat and Mass Transfer, 2005. **48**(25): p. 5112-5120.

[9] Giani, L., G. Groppi, and E. Tronconi, Heat Transfer Characterization of Metallic Foams. Industrial & Engineering Chemistry Research, 2005. **44**(24): p. 9078-9085.

[10] Yang, X.H., et al., A simplistic analytical unit cell based model for the effective thermal conductivity of high porosity open-cell metal foams. Journal of Physics D: Applied Physics, 2013. **46**(25): p. 255302.

[11] Jeng, T.-M., L.-K. Liu, and Y.-H. Hung, A Novel Semi-empirical Model for Evaluating Thermal Performance of Porous Metallic

Foam Heat Sinks. Journal of Electronic Packaging, 2004. **127**(3): p. 223-234.
[12] Karimi, N., Y. Mahmoudi, and K. Mazaheri, Temperature fields in a channel partially filled with a porous material under local thermal non-equilibrium condition – An exact solution. Proceedings of the Institution of Mechanical Engineers, Part C: Journal of Mechanical Engineering Science, 2014. **228**(15): p. 2778-2789.
[13] Vafai, K. and R. Thiyagaraja, Analysis of flow and heat transfer at the interface region of a porous medium. International Journal of Heat and Mass Transfer, 1987. **30**(7): p. 1391-1405.
[14] Nakayama, A.P., I, Momentum and heat transfer over a continuous moving surface in a non-Darcian fluid. Wärme - und Stoffübertragung, 1993. **28**(4): p. 177-184.
[15] Das, M.K., P.P. Mukherjee, and K. Muralidhar, Equations Governing Flow and Transport in Porous Media, in Modeling Transport Phenomena in Porous Media with Applications, M.K. Das, P.P. Mukherjee, and K. Muralidhar, Editors. 2018, Springer International Publishing: Cham. p. 15-63.
[16] Huang, H. and J.A. Ayoub, Applicability of the Forchheimer Equation for Non-Darcy Flow in Porous Media, in SPE Annual Technical Conference and Exhibition. 2006, Society of Petroleum Engineers: San Antonio, Texas, USA. p. 14.
[17] White, F.M., Viscous Fluid Flow. 2006, India: McGraw Hill. 629.
[18] Toolbox, E. Air - Prandtl Number 2018 [cited 2019 5/11/2019]; Available from: https://www.engineeringtoolbox.com/air-prandtl-number-viscosity-heat-capacity-thermal-conductivity-d_2009.html.
[19] Thermophysical Properties: Engine Oil. 2011 11/13/2011 [cited 2019 5/22/2019]; Available from: https://www.thermalfluidscentral.org/encyclopedia/index.php/Thermophysical_Properties:_Engine_Oil,_Unused.
[20] Kwarteng, A. A., 2019. A Similarity Solutions Approach to Forced Convection Heat Transfer Enhancement by Using Porous Media. PhD Thesis, Greensboro: North Carolina Agricultural and Technical State University, 124.